

Local triple-combination therapy results in tumour regression and prevents recurrence in a colon cancer model

João Conde^{1,2*}, Nuria Oliva¹, Yi Zhang¹ and Natalie Artzi^{1,3,4*}

Conventional cancer therapies involve the systemic delivery of anticancer agents that neither discriminate between cancer and normal cells nor eliminate the risk of cancer recurrence. Here, we demonstrate that the combination of gene, drug and phototherapy delivered through a prophylactic hydrogel patch leads, in a colon cancer mouse model, to complete tumour remission when applied to non-resected tumours and to the absence of tumour recurrence when applied following tumour resection. The adhesive hydrogel patch enhanced the stability and provided local delivery of embedded nanoparticles. Spherical gold nanoparticles were used as a first wave of treatment to deliver siRNAs against *Kras*, a key oncogene driver, and rod-shaped gold nanoparticles mediated the conversion of near-infrared radiation into heat, causing the release of a chemotherapeutic as well as thermally induced cell damage. This local, triple-combination therapy can be adapted to other cancer cell types and to molecular targets associated with disease progression.

Cancer is the leading cause of mortality worldwide, with over 10 million new cases every year in Europe and the US. It is estimated that 3 million new cases will be diagnosed with 1.7 million deaths each year¹. The need for the development of more effective cancer diagnostics and therapeutics is imperative. In fact, dire consequences pursue the massive investment in cancer therapy and in particular drug development, unlike the progress in treating other chronic diseases, resulting in high mortality each year worldwide. Colorectal cancer (CRC) is the second most common cause of cancer death among men and women in Europe, as stated by the World Health Organization. It is the third most common cancer found in the US, as specified by the American Cancer Society and the National Cancer Institute. After breast cancer, CRC is the second most common cancer in women and the third most frequent in men, after lung and prostate cancer. Overall, the lifetime risk of developing CRC is about 1 in 20 (ref. 2).

Surgery, referred to as colectomy or a segmental resection, is often the main treatment for early and late stage CRC. A reasonable proportion of CRC patients remain clinically remissive for months or years following tumour resection and chemotherapy. However, after this stage of remission, tumours recur in 30–50% of all cases, generally presenting metastasis. Moreover, surgery is fraught with many complications including bleeding at the surgical site, the formation of blood clots in the legs, and damage to nearby organs. Leakage from the anastomotic site is another complication that may lead to infection, delaying further treatment. Compromised healing following surgery may lead to scar tissue and bowel obstruction along with tissue adhesions³.

Previous therapies for CRC have not provided sufficient specificity and structural guidance to promote tumour inhibition after remission and the full regeneration of the injured intestinal tissue after surgery. Conventional cancer therapy involves the

use of anti-neoplastic agents that do not significantly distinguish between cancer and normal cells⁴. Efficient *in vivo* uptake to cancer cells requires better targeting moieties to improve cellular uptake and reduced toxicity to contiguous normal cells, towards reduced systemic toxicity and undesired side effects⁵.

This is where nanotechnology comes into play. Nanotechnology has immensely progressed in the last 20 years to supply important advances in early diagnosis and prevention, bioimaging, multifunctional therapies, and potent gene and drug delivery systems^{6–10}.

Here, we developed a hydrogel patch for local CRC treatment using triple-combination therapy: gene, drug and phototherapy. We hypothesized that a multi-modal approach is necessary to efficiently abrogate the tumour. Efficacious gene and drug delivery along with tumour ablation by phototherapy was achieved by coating the colorectal tumour with an adhesive hydrogel scaffold¹¹ made of oxidized dextran and poly(amidoamine) G5 dendrimer that we have shown are capable of enhancing the stability of doped nanoparticles used for local drug and gene delivery^{6,12,13}. We previously reported on the contextual performance of dendrimer/dextran adhesive hydrogel when applied to tissues with underlying pathology compared with healthy tissues and how to exploit tissue microenvironmental characteristics to inform rational material design^{11,14,15}. We now aim to take these precision biomaterials a step further, where materials are not only designed to attain predictive performance in pathological environments, but are used to attain complete tumour regression and reverse disease-specific traits to prompt selective and personalized therapies.

By developing a combination therapeutic approach that considers the tissue microenvironment in material design, we can achieve disease-responsive materials promoting selective uptake, oncogene modulation, drug release in cancer cells, and selective

¹Massachusetts Institute of Technology, Institute for Medical Engineering and Science, Cambridge, Massachusetts 02139, USA. ²School of Engineering and Materials Science, Queen Mary University of London, London E1 4NS, UK. ³Broad Institute of MIT and Harvard, Cambridge, Massachusetts 02142, USA.

⁴Department of Medicine, Division of Biomedical Engineering, Brigham and Women's Hospital, Harvard Medical School, Boston, Massachusetts 02115, USA. *e-mail: jconde@mit.edu; nartzi@mit.edu

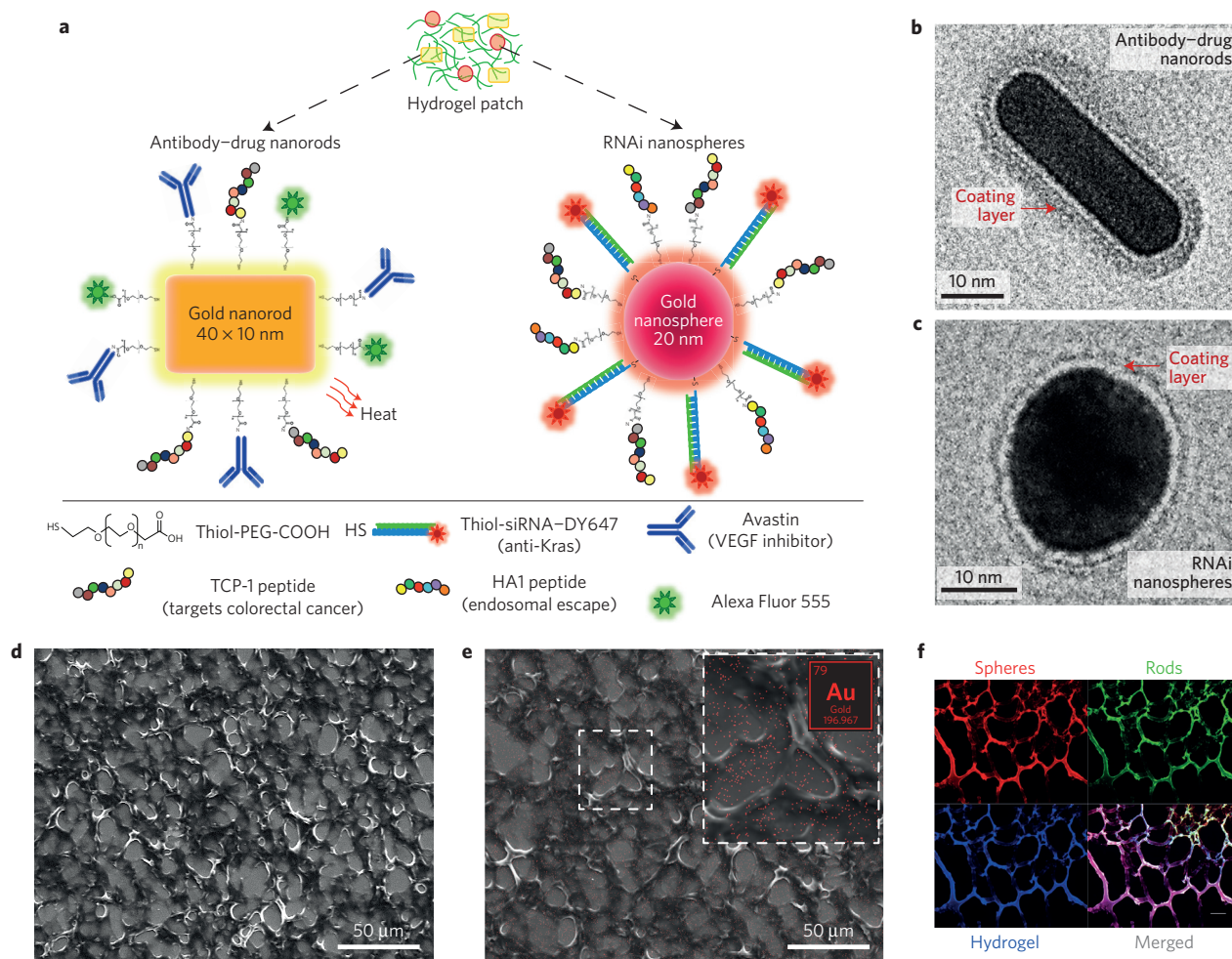


Figure 1 | The rationale behind the design of local triple-combination therapy. **a**, Drug-gold nanorods and siRNA-gold nanospheres doped in implantable hydrogels for local drug/gene delivery and local hyperthermia. **b,c**, Transmission electron micrographs of gold nanorods with an aspect ratio of 4.1 (40 × 10 nm) (**b**) and gold nanospheres with 20 nm diameter (**c**). The red arrows point to the negative staining of the coating layer. **d,e**, High-resolution SEM (**d**) and SEM/energy-dispersive X-ray (**e**) images of dextran-dendrimer hydrogel scaffolds. The gold content embedded in the hydrogels can be better appreciated in the magnified image (**e**, inset). **f**, Cryosection of dextran-dendrimer adhesive hydrogel (12 μm thickness) where dextran aldehyde from the hydrogel is labelled with Alexa Fluor 405 (in blue), RNAi nanospheres are tagged with DY647 (in red) and drug gold nanorods are labelled with Alexa Fluor 555 (in green).

phototherapy promoting tumour ablation, thus minimizing side effects. This modular platform is based on two waves of treatment; the knockdown of important genes in cancer progression followed by the delivery of a potent drug to stop cancer cell proliferation in several stages of the disease following triggered drug release with near-infrared (NIR) phototherapy. We demonstrate that this platform can be used as a prophylactic hydrogel patch to prevent cancer recurrence, and/or as a neoadjuvant therapy to shrink tumours before resection, thus eliminating the need for resection.

The design of local triple-combination therapy

Our specific goal and overall hypothesis was that the development of a hydrogel-based patch doped with nanoparticles for *in vivo* local triple therapy, gene/drug delivery combined with phototherapy, would synergistically abrogate tumours and prevent their recurrence, either with or without tumour resection. Platform efficacy was examined in an *in vivo* mouse model of CRC. A tunable hydrogel patch impregnated with drug- and siRNA-nanoparticle conjugates (drug-gold nanorods and short interfering RNA (siRNA)-gold nanospheres) for local gene and drug release in colorectal tumour cells was designed (Fig. 1a). Nanoparticles (that is, gold nanorods) were functionalized with biomolecules

that target unique or overexpressed biomarkers in tumour cells (tumour-targeting moieties) to enhance the uptake of gold nanorods in cancer cells. Gold nanorods, having the capacity to convert NIR radiation into heat causing localized release and tumour ablation^{16–18}, were functionalized with the Food and Drug Administration (FDA)-approved monoclonal antibody, bevacizumab or Avastin, that blocks the vascular endothelial growth factor (VEGF) pathway in CRC¹⁹. Bevacizumab (Avastin) neutralizes VEGF and blocks its signal transduction through VEGFR-1 and VEGFR-2 receptors, as demonstrated by the inhibition of VEGF-induced cell proliferation, survival, permeability, nitric oxide production, migration and tissue factor production²⁰. By inhibiting VEGFR activity we were able to block the endogenous expression of VEGF and to reduce the amount of secreted VEGF²⁰. The particles will release the drug (Avastin) and produce heat following laser irradiation to kill remaining cancer cells. TCP-1 peptide (N-CTPSPFHC-C), which is commonly used to target the vasculature of orthotropic CRC patients²¹ and specifically targets CRC cells, was conjugated to the nanorods and the nanospheres to provide preferential uptake in cancer cells. Gold nanospheres were used in conjunction with the nanorods to deliver siRNAs that silence a major oncogene driver

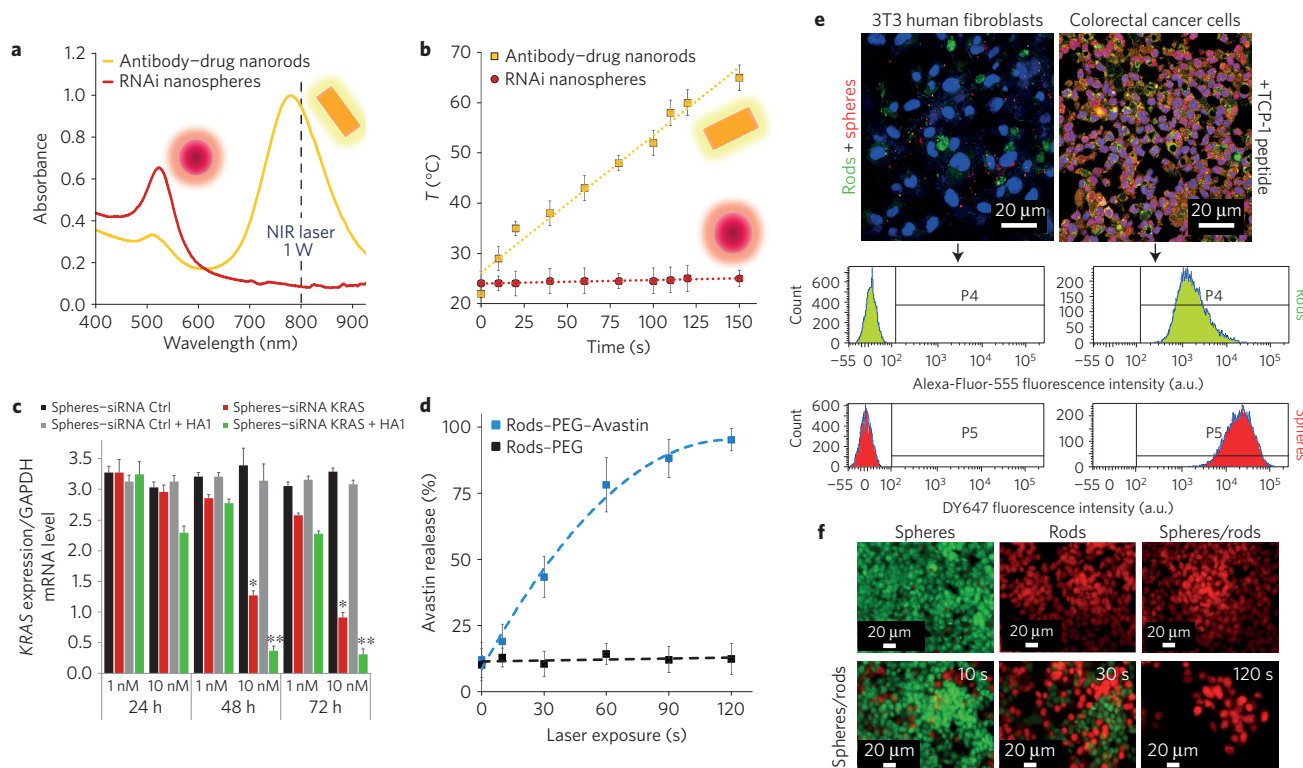


Figure 2 | Functional characterization and *in vitro* performance. **a**, Spectra for drug-gold nanorods (yellow) and siRNA-gold nanospheres (red) at equal gold concentrations. **b**, Rate of temperature escalation for drug-gold nanorod (yellow) and siRNA-gold nanosphere (red) solutions irradiated with a 808 nm laser at 1 W. **c**, *Kras* expression in LoVo-Luc CRC cells at 24, 48 and 72 h of incubation with 1 and 10 nM siRNA-gold nanospheres functionalized with and without the HA1 peptide ($n = 3$, statistical analysis was performed with a two-tailed Student's *t*-test, **, $P < 0.01$; *, $P < 0.05$). *Kras* levels were normalized to the *GAPDH* reference gene. **d**, Avastin (that is, drug) release from gold nanorods following increasing exposure to laser (10–120 s). **e**, Confocal microscope images and analytical flow cytometry of cellular uptake of drug-gold nanorods (in green) and siRNA-gold nanospheres (in red) by human 3T3 fibroblasts and LoVo-Luc CRC cells. **f**, Live-dead staining of CRC cells after uptake with drug-gold nanorods, siRNA-gold nanospheres or the combination 24 h after the application of a 808 nm laser at 1 W for increasing irradiation duration (red, dead cells; green, live cells). All experiments were done in triplicates and errors are reported as standard deviation (s.d.).

in CRC progression—*Kras* (Kirsten rat sarcoma viral oncogene homolog). *Kras* is an effector molecule responsible for signal transduction in CRC and approximately 30–50% of colorectal tumours are known to have a mutated *Kras* gene²². To enhance the siRNA uptake, the gold nanospheres were functionalized with an HA1 peptide (in addition to TCP-1), a fusogenic peptide (influenza haemagglutinin—HA1 peptide, N-YPYDVPDYA-C²³) that destabilizes the endosomal membrane stimulating endosomal discharge by a pH-responsive machinery.

Concerning the physico-chemical properties of the final nanoconjugates, the siRNA/nanoparticle ratio for the gold nanospheres was 105:1 and the Avastin (drug)/nanoparticle ratio for the gold nanorods was 15:1 (see Supplementary Table 1). The mean particle diameter of the siRNA-gold nanospheres was 32.7 (± 1.9) nm, and 35.6 (± 2.1) nm for the drug-gold nanorods, as measured by dynamic light scattering (DLS). Both siRNA-gold nanospheres -29.4 (± 5.2) mV and drug-gold nanorods -23.1 (± 3.8) mV are anionic as measured by the zeta potential.

Implantable dendrimer-dextran hydrogels will be doped with the drug-gold nanorods (Fig. 1b) and siRNA-gold nanospheres (Fig. 1c) to afford local drug/gene delivery and hyperthermia. Since delivery of these potent effector molecules will be preferentially achieved in tumoral cells, only minor damage to surrounding cells if at all should be conceivable, thus diminishing unnecessary death of surrounding healthy tissue. Extensive quantification (Supplementary Figs 1–4), stability (Supplementary Fig. 5) and characterization assays (Supplementary Figs 6 and 7) were conducted for the functionalized nanoconjugates.

To enable local release to diseased tissue while avoiding material migration and release to adjacent sites, the hydrogel was decorated with aldehyde groups (provided by the oxidized dextran) that interact with tissue amines to form adhesive bonds^{15,24}. The adhesive architecture was evaluated by high-resolution scanning electron microscope (SEM, Fig. 1d) images. In addition to the SEM images, we performed an energy-dispersive X-ray spectroscopy map-scanning analysis of the hydrogel doped with both drug-gold nanorods and siRNA-gold nanospheres to evaluate their elemental composition, especially the gold content, which pointed at a uniform particle distribution throughout the hydrogel (Fig. 1e).

Functional characterization and *in vitro* performance

Gold nanorods provide us with an efficacious photothermal tumour therapy^{25,26}. Hence, we evaluated the photothermal performance of gold nanorods when embedded in our hydrogel as a prophylactic thermal patch. It is well known that gold nanorods with 40×10 nm present an absorbance peak in the NIR (around 800 nm), whereas gold nanospheres with 20 nm diameter have a surface plasmon resonance peak around 530 nm (Fig. 2a). Therefore, we envisioned that when irradiated in the NIR range, only the gold nanorods would transduce electromagnetic radiation into heat. To evaluate the thermal effects of both gold nanorods and gold nanospheres using a NIR laser light source (808 nm, 1 W) and their potential to serve as photothermal probes *in vivo*, the temperature of gold nanorods and gold nanospheres (Fig. 2b) in aqueous solution was evaluated over time. Gold nanorod solution (10 nM) irradiation for

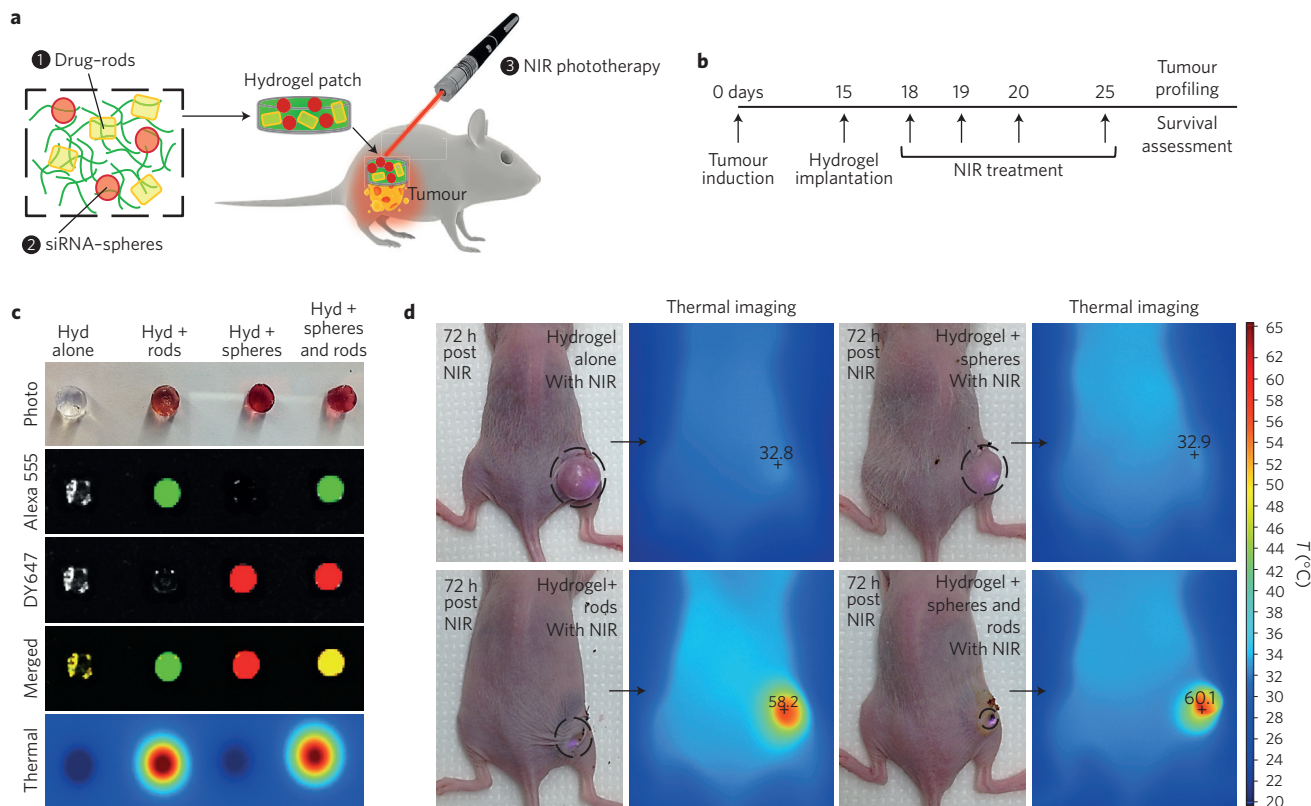


Figure 3 | Selective and efficient local triple therapy improves CRC therapeutic efficacy. **a**, Development of a smart hydrogel-nanoparticle patch as a prophylactic scaffold agent for *in vivo* local gene/drug delivery combined with phototherapy, before and after surgical removal of the tumour in an *in vivo* mouse model of CRC. A tunable hydrogel patch impregnated with drug-gold nanorods and siRNA-nanoparticle conjugates (drug-gold nanorods and siRNA-gold nanospheres) for local gene and drug release in colorectal tumoral cells was designed. **b**, Experiment flow: on day 0, CRC cells were injected into mice ($n = 5$ per group). Tumour volumes were monitored and on day 15 hydrogels were implanted. NIR treatment was applied at days 18, 19, 20 and 25 using a 808 nm laser at 1 W for 120 s. Mice were monitored in the following weeks for survival and tumour profiling. **c**, Fluorescence and thermographic images of the hydrogels doped with drug-gold nanorods, siRNA-gold nanospheres or their combination ($n = 5$). **d**, Thermographic surveillance of photothermal heating in mice ($n = 5$) implanted with hydrogels doped with drug-gold nanorods, siRNA-gold nanospheres or their combination, 72 h after the first NIR treatment.

120 s (808 nm, 1 W) resulted in a 50 °C rise in temperature, with no variation in temperature in the gold nanosphere solution following the same irradiation power. These results clearly demonstrate that the synthesized gold nanorods experience substantial thermal effects at low laser energy irradiation.

We then focused on examining the effect of siRNA-nanospheres on cancer cells' biochemical activity. At 24, 48 and 72 h post-transfection, quantitative PCR (qPCR) data confirmed a reduction in *Kras* expression with increasing amounts of siRNA-nanospheres (Fig. 2c). qPCR amplification of messenger RNA extracted from CRC cells (Lovo-6-Luc human colorectal adenocarcinoma cells) following treatment with siRNA-nanospheres confirmed the efficient RNA interference (RNAi) mechanism, as depicted by the decrease in target gene expression following treatment with siRNA-nanospheres. siRNA-nanospheres functionalized with the fusogenic peptide HA1 are more efficient in downregulating *Kras*, confirming the peptide function in enhancing nanosphere uptake and hence siRNA availability in the cytoplasm.

To corroborate the triggered conjugated drug release following heat-up of gold nanorods in cells, drug release was quantified as a function of increasing laser exposure time. Nearly 95% of the Avastin was released from the gold nanorods after 120 s of laser exposure (Fig. 2d). Studying the Avastin release mechanism (Supplementary Fig. 8) revealed that following NIR laser application the drug is being released while remaining conjugated to the PEG. Yet, the exposure to increasing temperatures following laser irradiation, under a range of exposure times, and the drug

attachment to the PEG do not affect Avastin activity in Lovo-6-Luc human CRC cells (Supplementary Fig. 9).

To evaluate cellular uptake, confocal microscopy was performed in Lovo-6-Luc CRC cells treated with the combination of DY647-labelled siRNA-nanospheres and Alexa Fluor 555-labelled drug-gold nanorods. Both siRNA-nanospheres and drug-nanorods have a high cellular uptake efficiency at 24 h post-incubation (Fig. 2e and Supplementary Fig. 10). Confocal imaging showed strong stability of both nanospheres and nanorods and efficient entry into the target CRC cells, when compared with the low cellular uptake in healthy 3T3 human fibroblasts. These results clearly demonstrate that both nanoparticles exhibit enhanced cellular uptake in cancer cells when conjugated to the TCP-1 peptide, when compared with healthy cells²¹.

A live-dead assay of CRC cells following uptake of 10 nM of spheres, rods or the combination of spheres and rods 24 h after laser application (Fig. 2f) or following increased exposure time to both nanoparticles was performed. This assay was conducted as previously described¹³ using a double staining procedure with acridine orange and propidium iodide representing green and red fluorescence for live and dead cells, respectively. As shown in Fig. 2f only drug-gold nanorods or the combination of rods and spheres results in a vast cell death (>95%) 24 h after laser application, due to the combination of local heat and consequent drug (Avastin) release.

To validate Avastin release from the gold nanorods and evaluate the efficacy of the drug in blocking VEGF, qPCR was performed with mRNA extracted from cells in the same conditions as described

above for the viability assays (Supplementary Fig. 11a). Notably, only the cells that were treated with gold nanorods carrying Avastin were able to inhibit VEGF expression 48 h after the application of an 808 nm laser light source for 120 s.

The tumorigenicity of the CRC cells was evaluated by measuring the IC₅₀ via an MTT assay (Supplementary Fig. 11b) following treatment with gold nanorods with and without drug and before or 24 and 48 h after laser irradiation. Gold nanorods with Avastin significantly inhibited CRC cell proliferation when compared with cells that were only laser irradiated or cells that were incubated with gold nanorods alone, without Avastin.

Local therapy improves cancer therapeutic efficacy

Next, we proceeded to study the *in vivo* nanoconjugates' pharmacokinetics and platform therapeutic efficacy in a CRC mouse model. The efficacy of the triple-therapy-based therapeutic platform was compared with gene, photo or chemotherapy alone and with or without the application of a NIR laser source. All therapeutic combinations, single, double or triple therapy, were performed with the same concentration of siRNA or drug and at the same therapeutic regimen.

Hydrogel scaffolds loaded with the specific therapeutic nanoconjugates were implanted adjacent to the colorectal tumour of SCID hairless congenic mice (CB17.Cg-Prkdc^{scid}Hr^{hr}/IcrCrI) when tumours reached a volume of ~100 mm³. In a combinatory wave of treatments, we were able to first knockdown an important gene in cancer progression. In a second wave of treatment, we delivered a potent drug to stop cancer cell proliferation following triggered drug release with NIR application, with concomitant tumour ablation using local phototherapy (Fig. 3a,b).

To form a hydrogel, 12.5% poly(amidoamine) G5 dendrimer (25% amines) solution was mixed with nanoparticle-containing 5% dextran aldehyde solution (drug–gold nanorods and/or siRNA–gold nanospheres were at a final concentration of 10 nM each). Drug–gold nanorod and siRNA–gold nanosphere scaffolds showed complete release within 24 h (Supplementary Fig. 12) under physiological conditions *in vitro* (pH 7.4 and 37 °C). These therapeutic hydrogels loaded with specific nanoconjugates for each therapy were monitored by fluorescence and thermographic imaging (Fig. 3c).

Having observed the hydrogels' photothermal efficiency (Fig. 3c), their ability to serve as powerful optical nanoantennas for photothermal tumour heating 72 h after NIR application was subsequently investigated (Fig. 3d). Hydrogel alone, hydrogel doped with drug–gold nanorods or siRNA–gold nanospheres or their combination (rods and spheres) was implanted into mice-bearing colorectal tumours. Temperatures above 60 °C occurred only in irradiated tumours containing hydrogels doped with drug–gold nanorods or rods and spheres together (Fig. 3d), whereas hydrogel alone or hydrogel doped with siRNA–gold nanospheres displayed maximum surface temperatures of around 33 °C.

Tumour regression and recurrence prevention

The capability of the triple therapy to shrink the tumour before its resection or prevent tumour recurrence following resection was evaluated in two separate mouse groups; hydrogel containing both drug–gold nanorods and siRNA–gold nanospheres was implanted on top of the tumour before its resection or at the tumour site following resection as a wash-out procedure. Inhibition of tumour progression was measured by luciferase expression, as previously described⁶, while nanoconjugates' release (drug–gold nanorods in green and siRNA gold nanospheres in red) was tracked fluorescently (Fig. 4a) via a live imaging system for 15 days after hydrogel implantation and 10 days after the first NIR application.

Nanoconjugate uptake was quantified using intermittent fluorescence imaging of live mice for 15 days post-implantation, and their biodistribution by the fluorescent signal of excised organs

(liver, kidneys, spleen, heart, lungs and intestines) (Fig. 4a for triple-therapy groups and Supplementary Figs 13–15 for all other treatment combinations). No fluorescent signal was detected in any of the major organs. All nanoconjugates accumulate exclusively in the tumour tissue as demonstrated by the *ex vivo* images of the organs (Fig. 4a and Supplementary Figs 13–15).

When the patch was used as a prophylactic measure following tumour resection, complete remission was achieved (Fig. 4a,c). Even when the tumour was not resected, application of the hydrogel patch resulted in tumour abrogation as evident by bioluminescence imaging (more than 90%, $n = 5$, $P < 0.001$) 15 days after hydrogel implantation, eliminating the need for resection (Fig. 4a,b). We found that 40% of the tumours recurred following resection in the absence of further treatment (hydrogel alone control group), while the triple-therapy hydrogels implanted post-resection were able to completely destroy the remaining cancer cells, thus preventing tumour re-growth (Fig. 4a,c and Supplementary Fig. 16). This effect was perpetual as 170 days after tumour resection there was still no evidence for tumour recurrence in the triple-therapy hydrogel group (Supplementary Fig. 16). When comparing the efficacy of single, dual or triple therapy (that is, single therapy: chemotherapy, gene therapy or phototherapy; dual therapy: gene therapy and chemotherapy, chemotherapy and phototherapy or gene therapy and phototherapy; or triple therapy: chemotherapy, gene therapy and phototherapy), the triple therapy is far more efficacious than the other therapies or their combinations thereof (Fig. 4d). Irrespective of treatment modality, phototherapy add-on resulted in increased nanoparticle accumulation in the tumour both for nanorods and for nanospheres, as was quantified by their respective fluorescence signal in mouse tissues using a live imaging system at day 15 after single, dual or triple therapy (Supplementary Fig. 17). The combination of relatively instantaneous killing of cancer cells following phototherapy with high accumulation of nanoparticles containing drug/gene may result in a 'higher effective dose' of the cargo per cell, which further contributes to tumour abrogation.

To further demonstrate the superiority of the triple-therapy local hydrogel patch, the efficacy of the local delivery was compared with systemic (tail-vein injection) or intratumoral administration of the nanoparticles alone, with drug–gold nanorods and/or siRNA–gold nanospheres at a final concentration of 10 nM each (Supplementary Figs 18 and 19). We found that while the local administration of a hydrogel patch doped with triple-therapy combination resulted in more than 90% tumour shrinkage (Fig. 4d), only 60% or 40% tumour reduction was attained following intratumoral and systemic administration of the same therapy combination, respectively (Supplementary Fig. 19b), leading to poor survival increments (36 days after tumour induction for systemic therapy, 41 days for intratumoral injection and at least 150 days for the local hydrogel therapy, see Supplementary Fig. 19c). Systemic administration of the nanoparticles results in nonspecific accumulation in the kidneys, spleen and liver (Supplementary Fig. 19a). These results provide convincing evidence that the hydrogel patch is instrumental to the achievement of superior therapeutic performance.

To validate the safety of the hydrogel patches mice organs were harvested 15 days after hydrogel implantation and H&E stained for histopathology (Supplementary Fig. 20). H&E staining revealed that *in vivo* application of hydrogel alone or the triple-therapy hydrogels did not cause any organ damage (that is, lung, liver, kidney, spleen, heart, intestine), when compared with the control group (without hydrogel treatment). Nevertheless, the tumour tissue shows extensive reduction in vascularization, in accordance with tumour size reduction following treatment. No signs of *in vivo* toxicity nor other physiological complications were observed in any of the animals for 15 days after hydrogel exposure as indicated by the preservation of steady body weight (Supplementary Fig. 21), pointing at hydrogel biocompatibility.

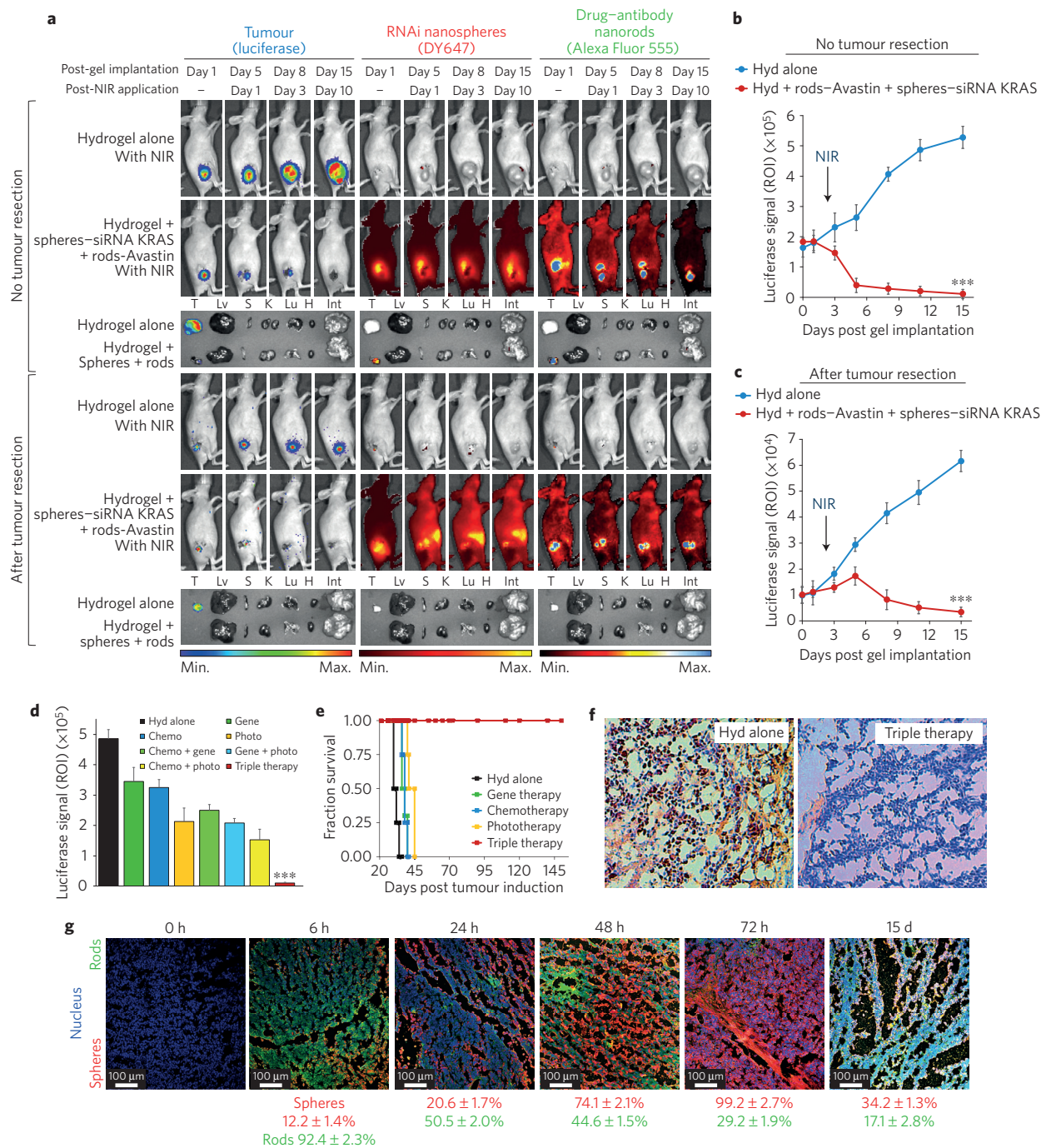


Figure 4 | Local triple-therapy combination results in complete tumour regression and recurrence elimination before and after tumour resection, respectively. **a**, Live imaging of SCID hairless congenic mice with colorectal tumour xenografts implanted with hydrogels that are embedded with drug-gold nanorods and siRNA-gold nanospheres with NIR treatment, either with no tumour resection or after tumour resection ($n = 5$ per group). *Ex vivo* images of tumours and whole body organs (T, tumour; Lv, liver; K, kidneys; S, spleen; H, heart; Lu, lung; Int, intestines) are also depicted. **b, c**, Tumour burden following treatment as measured by luciferase activity, without tumour resection (**b**) and after tumour resection (**c**) ($n = 5$, statistical analysis was performed using two-way analysis of variance, $***, P < 0.001$). Errors are reported as standard deviation (s.d.). **d**, Tumour burden of mice treated with gene therapy (siRNA-gold nanospheres), chemotherapy (drug-gold nanorods), phototherapy (gold nanorods) or double (chemo + gene, gene + photo, chemo + photo) and triple therapy (gene, chemo and phototherapy combination) ($n = 5$, statistical analysis performed with two-way analysis of variance, $***, P < 0.001$), as measured by luciferase activity. Errors are reported as standard deviation (s.d.). **e**, Kaplan-Meier curves for mice treated with hydrogel scaffolds for gene therapy (siRNA-gold nanospheres), chemotherapy (drug-gold nanorods), phototherapy (gold nanorods) or triple therapy (gene therapy, chemotherapy and phototherapy combination). Statistical analysis ($n = 5$) was performed with a Log-Rank Mantel-Cox test ($P = 0.008$). Survival cutoff criteria included tumour ulceration or compassionate euthanasia, when the aggregate tumour burden > 1 cm in diameter, or if the tumour impeded eating, urination, defecation or ambulation. **f**, Immunohistochemical evaluation of Ki67 for tumours treated with hydrogels alone or following triple therapy (gene therapy, chemotherapy and phototherapy combination). **g**, Histopathology and biodistribution analyses of tumour tissue from mice treated with triple-therapy combination for several time points (from 6 h to 15 days) (blue, nucleus, DAPI; red, RNAi nanospheres, DY647; green, antibody-drug nanorods, Alexa Fluor 555). Scale bars, 100 μm . Quantification of nanoparticle percentage distribution over time was calculated using unity-based normalization.

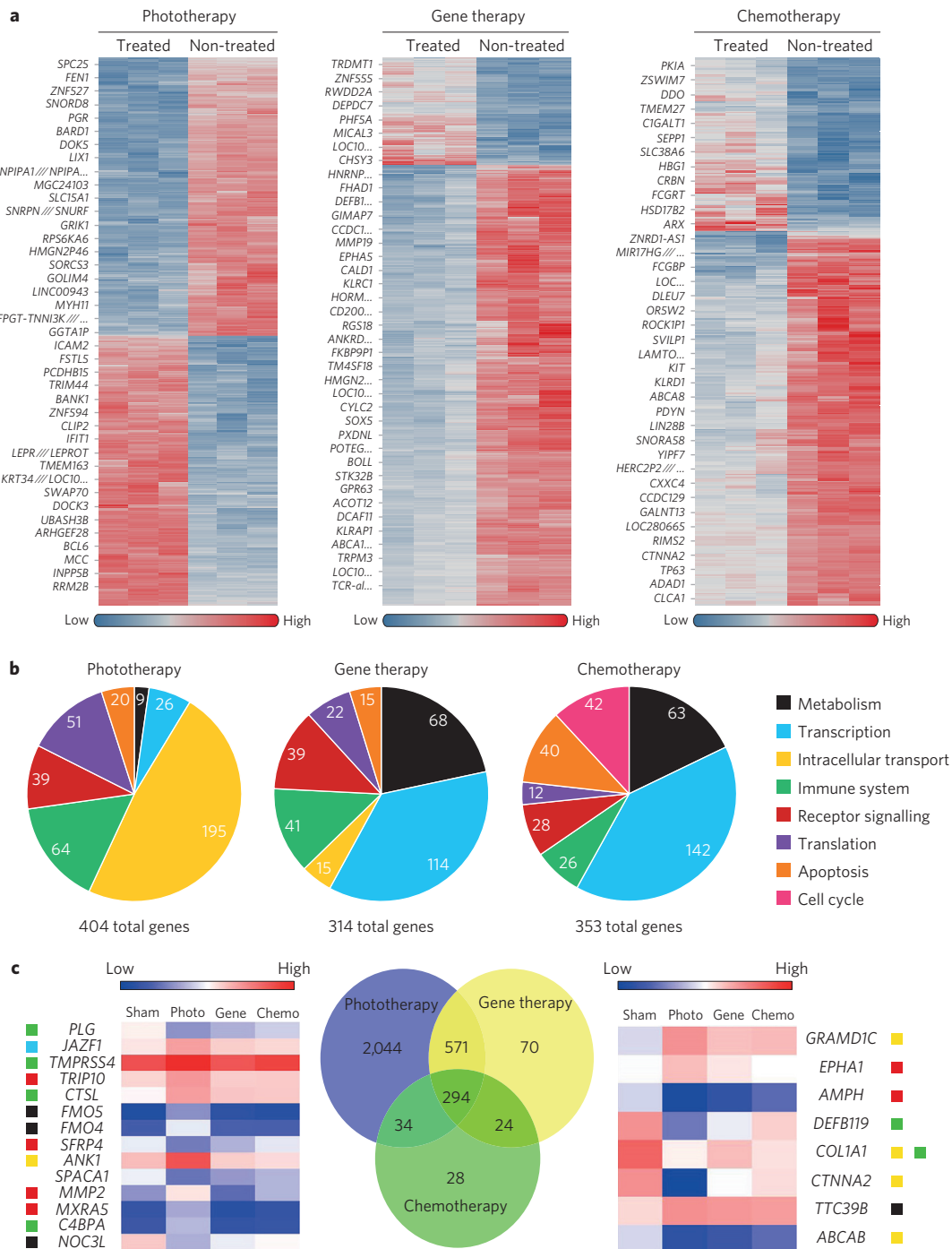


Figure 5 | Altered tumour genetic profile in response to local therapy treatment. **a**, Differential gene expression heat maps for GeneChip PrimeView Human Gene Expression Array of mice treated with gene therapy (siRNA-gold nanospheres) or chemotherapy (drug-gold nanorods) or phototherapy (gold nanorods) or triple therapy (gene, chemo and phototherapy combination), when compared with non-treated groups. **b**, Pathway analysis of significantly altered genes after single local therapy modalities: gene therapy, chemotherapy or phototherapy. **c**, Selection of potential gene targets (left, genes altered by phototherapy; right, genes altered by the three treatments) involved in tumour regression in response to local therapies. The whole-genome data are representative from three different tumours.

Survival study was performed for mice following triple therapy (gene therapy, chemotherapy and phototherapy combination) or control single therapies (gene therapy: siRNA-gold nanospheres; chemotherapy: drug-gold nanorods; or phototherapy: gold nanorods). Significant high mouse survival advantage followed triple therapy compared with hydrogel alone, or the single-therapy groups (Fig. 4e) ($P = 0.008$, 100% survival for at least 170 days). Survival follows the same trend seen with tumour size reduction

following the different treatment modalities (see Fig. 4a). This data are of utmost importance since patients that present with CRC will undergo surgery to resect the tumour and in more advanced stages undergo chemotherapy, but still carry the risk of recurrence owing to remaining cells at the tumour resection site that will continue to proliferate^{27,28}.

Immunohistochemical analysis showed that Ki67 expression, which is a cellular marker exclusively linked with cell proliferation,

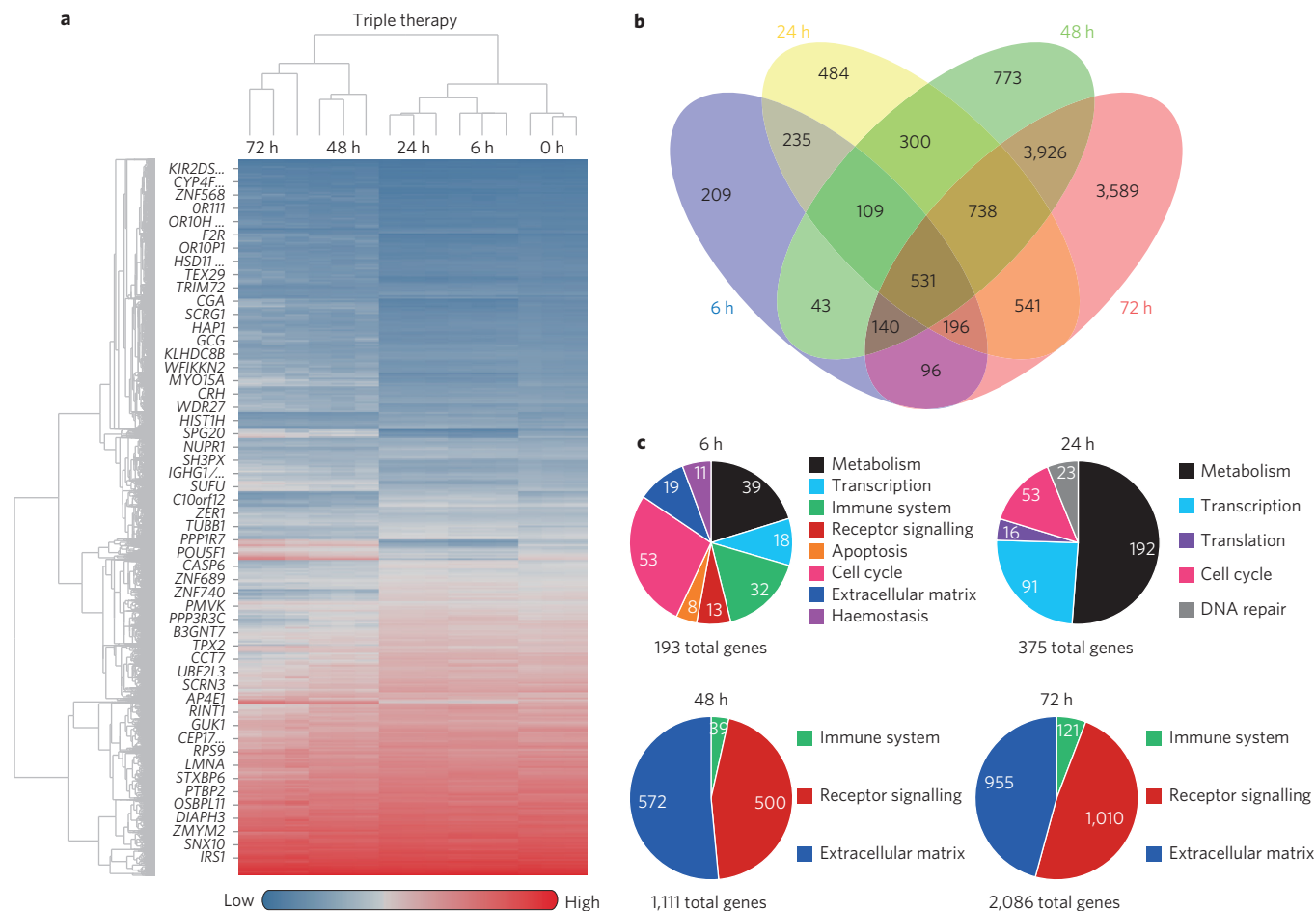


Figure 6 | Canonical pathway kinetics in triple-therapy combination. **a**, Differential gene expression heat maps for GeneChip PrimeView Human Gene Expression Array of mice treated with triple therapy (gene therapy, chemotherapy and phototherapy combination), for different time points of treatment: 6, 24, 48 and 72 h. **b**, Venn diagram from the differential gene expression heat maps of mice treated with triple therapy at different time points post-treatment. **c**, Pathway analysis of significantly altered genes after local combination triple therapy at different time points post-treatment. Selection of potential gene targets involved in tumour regression in response to local triple therapy over time. The whole-genome data are representative out of three different tumours.

was considerably reduced following local triple therapy when compared with the hydrogel-alone group (Fig. 4f).

Histologically, both drug–gold nanorods (in green) and siRNA–gold nanospheres (in red) were able to accumulate efficiently throughout the tumour tissue over time (Fig. 4g). Interestingly, nanorods present with more substantial accumulation early (peak at 6 h, $92.4 \pm 2.3\%$ accumulation) followed by nanosphere accumulation (peak at 72 h, $99.2 \pm 2.7\%$ accumulation). These findings corroborate the results seen in Fig. 4a, where all nanoconjugates accumulate exclusively in the tumours.

Tumour genetic profile in response to single local therapy

Following assessment of therapeutic efficacy, we studied the tumour genetic profile of treated mice since the gene expression profile of a cell determines its phenotype as well as its response to various factors, including drugs, irradiation or gene modulators²⁹. To understand host response to local administration of the therapeutic hydrogel doped with nanoparticles, colorectal tumour gene expression profiles in mice were generated using a GeneChip PrimeView Human Gene expression array. These arrays contain more than 530,000 probes housing over 36,000 transcripts and variants, which reproduce more than 20,000 genes that are plotted through RefSeq or via UniGene annotation. For gene expression heat maps, the average expression across three independent

replicates in each condition based on the probes with the maximum signal intensity per gene was calculated.

A clustergram of genes that are differentially expressed following the application of hydrogel scaffolds for gene therapy (siRNA–gold nanospheres), chemotherapy (drug–gold nanorods) or phototherapy (gold nanorods) in mice was generated (Supplementary Fig. 22a). The data were analysed by unsupervised hierarchical clustering, which showed that the three treatment groups had distinct gene expression profiles. Using a threefold change relative to the sham group (that is, treatment with hydrogel alone) as a benchmark for differential expression, numerous genes were derived from the different therapeutic modalities. Responders (that is, phototherapy) were clustered separately from non-responders (gene therapy and chemotherapy) and untreated samples (that is, sham). For the clustering of differentially expressed genes, a total of 20,087 genes were analysed and an absolute \log_2 fold change of ≥ 1 with an adjusted p value of ≤ 0.05 to define the differentially expressed gene sets was used. For the correlation between the untreated group and the phototherapy group the number of differential genes is 2,943, for the gene-therapy group 959 and for the chemotherapy group 380 genes (Supplementary Fig. 22a). The volcano plots for the different therapies were assembled by plotting the negative log of the p value on the y axis. Highly deregulated genes appear further to the left and right

sides, whereas highly significant changes appear higher on the plot (Supplementary Fig. 22).

To identify the relationship between the four ordered sets of treatments (in this case, gene expression data for several different therapies and for the untreated group—sham) a Pearson correlation matrix was developed (Supplementary Figs 22b and 24). This matrix indicates both how the four sets are related and the strength of that relationship. All replicates correlate very well (the diagonal of the heat map), and all different therapy samples show a very high correlation (>0.95).

To evaluate which genes are up- or downregulated in response to the different treatments we created a set with \log_2 fold-change cutoff of ≥ 2 and realized a hierarchical clustering of these differentially expressed gene sets, using a row-normalized data-set that was prepared using the broad GenePattern tool Pre-process Dataset³⁰ (Fig. 5a).

This analysis enables pinpointing distinct gene expression fluctuations related to phototherapy with several clusters of genes that were only suppressed or induced in these groups (Fig. 5a). For example, phototherapy-treated tumours showed substantial suppression of a large cluster of genes that are involved in cytoskeleton remodelling and cell adhesion via integrin-mediated cell adhesion or involved in cell proliferation and differentiation such as *MYH11* (myosin heavy chain). However, a large cluster of genes was induced only in the phototherapy-treated tumours. This cluster contains genes mainly involved in metabolism such as *RRM2B* (ribonucleotide reductase M2 B), or in immune response mechanisms such as *Bcl-6* (B-cell CLL/lymphoma 6).

Concerning gene therapy, the major difference is the presence of a large cluster that is repressed in response to treatment. This includes genes mainly involved in protein folding, membrane trafficking and signal transduction, such as *ABCA1* (ATP-binding cassette, sub-family A).

We also found that the response to chemotherapy was associated with the depletion of several genes related to metabolism such as *ADH6* (alcohol dehydrogenase 6) or in cell adhesion and migration processes such as *FNI* (fibronectin).

Using an alternative clustering/filtering, we selected the top 25 largest absolute fold-change genes for each of the three therapy groups, and then summarized the selection into a string. Briefly, YesYesYes would be top 25 in all three therapy groups, YesNoNo is the top 25 in phototherapy groups but not in gene therapy or chemotherapy groups (Supplementary Fig. 25). These results revealed that there are 59 genes that are top 25 in at least 1 therapy group. Most importantly, this analysis revealed that several microRNA (miRNAs; that is, miR-17, miR-18A, miR-19A, miR-19B1, miR-20A and miR-92A1) are downregulated in all therapy groups, whereas in the control group (sham) they are all upregulated. These miRNAs are part of the miR-17~92 cluster, which encodes for six individual miRNAs: miR-17, miR-18A, miR-19A, miR-20A, miR-19B1 and miR-92A1. The miR-17~92 miRNA cluster is positioned on human chromosome 13q31.3, in a genomic region that is frequently activated in lymphomas and other types of cancer³¹. The mature miRNAs encoded by this locus are highly expressed in cancer cells promoting cell proliferation and blocking apoptosis³² and have key roles in cancer progression due to their capability of suppressing the expression of numerous tumour-associated proteins³³.

Supervised Gene Ontology (GO) and detailed Kyoto Encyclopedia of Genes and Genomes (KEGG) pathway analysis was used to identify the molecular pathways and describe the biological processes of the transcript profiling data³⁴. Pathway analyses were performed using Gene Set Enrichment Analysis tools and were based on differentially expressed genes in each treatment group including phototherapy, gene therapy and chemotherapy compared with sham controls. Differential expression was defined

as multiple testing adjusted *p* values that are smaller than or equal to 0.05 and fold change greater than or equal to 1.5-fold by probes with the maximum intensity in each gene. The enrichment results with canonical pathway gene sets C2CP were reported and a false discovery rate (FDR) of 25% or less was used to select interesting gene sets for hypothesis generation.

Based on the GO analysis, the GO terms of 'biological process' that were significantly over-represented in each cluster of the heat maps are shown in Fig. 5b. The GO terms of the altered genes belong to multiple pathways mainly related with metabolism, intracellular transport mechanisms, receptor signalling, cell cycle and apoptosis, immune and defence response and transcription/translation processes. These observations confirm the distinct up- and downregulation of genes following the different therapeutic modalities, especially succeeding phototherapy.

We found that in response to phototherapy the molecular pathways involved were mainly regulated by genes controlling intracellular transport, such as membrane trafficking, whereas the mechanisms behind both gene therapy and chemotherapy approaches were mainly regulated by transcription (that is, chromatin organization) and metabolism (that is, metabolism of proteins, of amino acids, of nucleotides, of nitric oxide or of carbohydrates) (Fig. 5b and Supplementary Fig. 26).

To identify key genes involved in CRC that could be altered in response to each therapy, we used MetaCore; an integrated software suited for functional analysis of microarrays, based on a high-quality, manually curated database of signalling and metabolic pathways. By clustering the GO data using disease biomarkers via the calculation of the *p*-value distribution of the differentially expressed genes in each treatment group, we were able to identify deregulated pathways in response to each therapy. A Venn diagram shows that only phototherapy alone alters more than 2,000 genes, including 14 key genes that are associated with CRC progression that are activated in response to stress or to external stimuli, such as metabolism, receptor signalling and defence mechanisms. (Fig. 5c and Supplementary Fig. 26.) For example, *PLG* (plasminogen) whose activation leads to a decrease in apoptosis and tumour progression³⁵ is downregulated following phototherapy when compared with the sham, which is upregulated.

Another example is *SFRP4* (secreted frizzled-related protein 4), which is associated with the *Wnt* signalling and that is downregulated in response to phototherapy. It is well known that an abnormal regulation of the *Wnt* signalling pathway plays a key role in the onset and progression of CRC, as this pathway is activated in colon cancer cells³⁶.

Another gene that is highly upregulated in response to phototherapy is *ANK1* (ankyrin 1), which plays key roles in cytoskeleton remodelling and maintenance of specialized membrane domains.

When comparing all of the common genes and variants in the different treatment groups (Fig. 5c and Supplementary Fig. 27), we found that the majority of genes related to CRC progression were mainly associated with intracellular transport (for example, *CTNNA2*, which is a structural constituent of cytoskeleton and cadherin binding and that we found highly repressed in the phototherapy group alone), receptor signalling (for example, *EPHA1*, which is protein-tyrosine kinase that has been implicated in colorectal carcinogenesis³⁷ and that we found slightly upregulated in the phototherapy group), or immune system (for example, *DEFB119*, which is a β -defensin and a diagnostic markers in CRC³⁸ that was highly repressed in the phototherapy group alone). The qPCR validation of the expression levels of these genes is depicted in Supplementary Fig. 28. These results are in concordance with the microarray results and further confirm the reliability and accuracy of the array chip approach.

The molecular pathways that determine the effectiveness of anti-tumour response following a specific therapy are poorly understood.

Our profiling analysis allowed us to identify potential intermediaries of tumour response to therapy. By employing a network analysis methodology, we could classify and rank numerous cores that were related to response to therapy. Specifically, whole-gene expression analysis of tumours from treated mice suggests that phototherapy treatment leads to the repression and induction of a higher number of genes and variants when compared with gene therapy or chemotherapy. Molecular pathways that are mainly regulated by genes controlling intracellular transport, such as membrane trafficking, were 'turned on' in response to phototherapy, whereas transcription and metabolism mechanisms were stimulated following both gene therapy and chemotherapy. Moreover, the gene expression analysis revealed that the efficacy of the treatment is correlated with the number of genes altered; the phototherapy group is highly efficacious in reducing tumour size (Fig. 4d) and increasing mouse survival (Fig. 4e) while inducing the highest number of altered genes (Fig. 5c).

Canonical pathway kinetics in local triple therapy

Gene expression data analysis provides insights into the contribution of each therapeutic modality to tumour abrogation. Nevertheless, the contribution of the combination of the three therapeutic modalities: gene therapy, chemotherapy and phototherapy, is a key element in studying the host response based on genome-wide microarray analysis. However, 15 days post-treatment with the triple-therapy hydrogel, the RNA in the excised tumours was completely degraded following irradiation (see Supplementary Fig. 29) and hence did not pass the quality check required for the microarray studies. Therefore, we conducted a series of *in vivo* experiments in which we followed the gene expression alteration succeeding triple therapy over time, providing information about the canonical pathway kinetics of the triple-therapy combination (Fig. 6).

Interestingly, tumour genetic profiles of mice treated with the triple therapy change over time (Fig. 6a). This is evident when we compare and contrast the altered genes in treated mice at 6, 24, 48 or 72 h. At the intersection of the genetic profiles of all the treatment groups there are more than 500 common genes (Fig. 6b). These genes are mainly associated with apoptosis and survival (Beta-2 adrenergic receptor) as well as stress response (serotonin receptor HTR1A), immune system (MAPK signalling), chemotaxis (that is, CCL16, CCL20, CXCL16 and CCL25) and regulation of extracellular matrix (matrix metalloproteinase (MMP) family).

Based on the GO analysis, the GO terms of the altered genes change over time (Fig. 6c) and increase in number. At 6 h, the majority of the altered genes belong to pathways that are mainly related to metabolism, cell cycle and apoptosis (downregulation of caspase-10 and upregulation of death receptors DR3, 4 and 5) and immune and defence responses (upregulation of IL-22, IL-1 and IL-4). At 24 h, there is a significant increase in altered genes related to metabolism (upregulation of cytochromes (CYPs) and hydroxysteroid dehydrogenases (HSDs)) and transcription (upregulation of histones H1, H2 and G-protein). At 48 and 72 h, the molecular pathways controlling the tumour cells shift completely to processes related to receptor signalling (downregulation of Ephrin receptors, EGFR and VEGF, this last due to the Avastin action, which neutralizes VEGF and blocks its signal transduction) and regulation of extracellular matrix (upregulation of E-cadherin, plasmin and MMPs, and downregulation of collagen III and IV). From 6 h to 72 h, the number of altered genes also changes from 209 to 3,589, which correlates with the maximum therapeutic efficacy observed after 72 h using the local triple-therapy combination (see Fig. 4). This proves that the genetic profile is determined by the therapeutic modality.

Taken together, the wide genome array assays from tumours in response to each of the single therapeutic modalities and especially to the triple-combination therapy provide potential biomarkers

for gene/drug/phototherapy in clinical application. The biomarkers identified herein via quantitative gene expression analysis may be used in the future to better design materials that can target specific genes/pathways to achieve better clinical outcome based on prognosis analysis and correlations between preclinical studies and patient-derived samples to choose the optimal disease-associated biomarkers. A comprehensive scrutiny of the genes in the tumour microenvironment in response to therapy as the ones realized herein should further drive the discussion on what 'cargos' a material should contain in light of the observed tumour microenvironment characteristics and response to therapy.

Outlook

Our work presents a rational treatment strategy following a comprehensive scrutiny of the tumour microenvironment and host response to different therapeutic modalities based on genome-wide microarray analysis. The triple-therapy patch (that is, gene therapy, chemotherapy and phototherapy combination) synergistically abrogates the tumour, facilitating complete prevention of colon cancer recurrence following resection, and complete tumour remission when applied to non-resected tumours. Our results demonstrate the superiority of local compared with systemic administration or intratumoral injections both in terms of tumour shrinkage and survival rate. We identified the molecular and genetic pathways triggered in response to the three therapeutic modalities—phototherapy, gene therapy and chemotherapy—by tumour gene expression profiling in treated mice. Tumour genetic profiles of triple-therapy-treated mice are associated with an increased number of altered genes, which correlates with therapeutic efficacy as measured by tumour size. Hence, biomaterials-based local therapy provides a platform for efficient cancer treatment and for the discovery of new therapeutic targets. Follow-up studies in large preclinical models would exploit colonoscopy equipment to deliver the material directly to the colonic tumour while enabling the material to cure *in situ*. This delivery approach would eliminate issues associated with laser penetration, as photothermal irradiation would occur directly at the tumour site. Utilizing minimally invasive techniques (for example, colonoscopy) to apply the triple-therapy platform and evaluate its efficacy would potentially improve clinical procedures and therapeutic outcomes.

Methods

Methods and any associated references are available in the [online version of the paper](#).

Received 10 December 2015; accepted 21 June 2016;
published online 25 July 2016

References

1. Siegel, R. L., Miller, K. D. & Jemal, A. Cancer statistics, 2016. *CA Cancer J. Clin.* **66**, 7–30 (2016).
2. Kistler, C. E. Colorectal-cancer incidence and mortality after screening. *N. Engl. J. Med.* **369**, 2354–2354 (2013).
3. Kountouras, J., Zavos, C. & Chatzopoulos, D. Therapy for colorectal cancer. *N. Engl. J. Med.* **352**, 1820–1821 (2005).
4. Minelli, C., Lowe, S. B. & Stevens, M. M. Engineering nanocomposite materials for cancer therapy. *Small* **6**, 2336–2357 (2010).
5. Liu, Y., Miyoshi, H. & Nakamura, M. Nanomedicine for drug delivery and imaging: a promising avenue for cancer therapy and diagnosis using targeted functional nanoparticles. *Int. J. Cancer* **120**, 2527–2537 (2007).
6. Conde, J., Oliva, N., Atilano, M., Song, H. S. & Artzi, N. Self-assembled RNA-triple-helix hydrogel scaffold for microRNA modulation in the tumour microenvironment. *Nature Mater.* **15**, 353–363 (2016).
7. Howes, P. D., Chandrawati, R. & Stevens, M. M. Colloidal nanoparticles as advanced biological sensors. *Science* **346**, 1247390 (2014).
8. Wu, S. Y., Lopez-Berestein, G., Calin, G. A. & Sood, A. K. RNAi therapies: drugging the undruggable. *Sci. Transl. Med.* **6**, 240ps7 (2014).

9. Bertrand, N., Wu, J., Xu, X., Kamaly, N. & Farokhzad, O. C. Cancer nanotechnology: the impact of passive and active targeting in the era of modern cancer biology. *Adv. Drug Deliv. Rev.* **66**, 2–25 (2014).
10. Conde, J., Edelman, E. R. & Artzi, N. Target-responsive DNA/RNA nanomaterials for microRNA sensing and inhibition: the jack-of-all-trades in cancer nanotheranostics? *Adv. Drug Deliv. Rev.* **81**, 169–183 (2015).
11. Oliva, N. *et al.* Regulation of dendrimer/dextran material performance by altered tissue microenvironment in inflammation and neoplasia. *Sci. Transl. Med.* **7**, 272ra211 (2015).
12. Segovia, N. *et al.* Hydrogel doped with nanoparticles for local sustained release of siRNA in breast cancer. *Adv. Healthc. Mater.* **4**, 271–280 (2015).
13. Conde, J., Oliva, N. & Artzi, N. Implantable hydrogel embedded dark-gold nanoswitch as a theranostic probe to sense and overcome cancer multidrug resistance. *Proc. Natl Acad. Sci. USA* **112**, E1278–E1287 (2015).
14. Artzi, N. *et al.* *In vivo* and *in vitro* tracking of erosion in biodegradable materials using non-invasive fluorescence imaging. *Nature Mater.* **10**, 704–709 (2011).
15. Artzi, N., Shazly, T., Baker, A. B., Bon, A. & Edelman, E. R. Aldehyde-amine chemistry enables modulated biosealants with tissue-specific adhesion. *Adv. Mater.* **21**, 3399–3403 (2009).
16. von Maltzahn, G. *et al.* Computationally guided photothermal tumor therapy using long-circulating gold nanorod antennas. *Cancer Res.* **69**, 3892–3900 (2009).
17. Huang, X., El-Sayed, I. H., Qian, W. & El-Sayed, M. A. Cancer cell imaging and photothermal therapy in the near-infrared region by using gold nanorods. *J. Am. Chem. Soc.* **128**, 2115–2120 (2006).
18. von, M. G. *et al.* Nanoparticles that communicate *in vivo* to amplify tumour targeting. *Nature Mater.* **10**, 545–552 (2011).
19. Sonpavde, G. Bevacizumab in colorectal cancer. *N. Engl. J. Med.* **351**, 1690 (2004).
20. Wang, Y., Fei, D., Vanderlaan, M. & Song, A. Biological activity of bevacizumab, a humanized anti-VEGF antibody *in vitro*. *Angiogenesis* **7**, 335–345 (2004).
21. Li, Z. J. *et al.* A novel peptide specifically targeting the vasculature of orthotopic colorectal cancer for imaging detection and drug delivery. *J. Control. Release* **148**, 292–302 (2010).
22. Sunakawa, Y., Lenz, H. J. & Ichikawa, W. RAS mutations in colorectal cancer. *N. Engl. J. Med.* **369**, 2159 (2013).
23. Bosch, F. X., Garten, W., Klenk, H. D. & Rott, R. Proteolytic cleavage of influenza-virus hemagglutinins—primary structure of the connecting peptide between Ha1 and Ha2 determines proteolytic cleavability and pathogenicity of avian influenza-viruses. *Virology* **113**, 725–735 (1981).
24. Oliva, N. *et al.* Natural tissue microenvironmental conditions modulate adhesive material performance. *Langmuir* **28**, 15402–15409 (2012).
25. Wang, Y. H. *et al.* Synergistic delivery of gold nanorods using multifunctional microbubbles for enhanced plasmonic photothermal therapy. *Sci. Rep.* **4**, 5685 (2014).
26. Kuo, W. S. *et al.* Gold nanorods in photodynamic therapy, as hyperthermia agents, and in near-infrared optical imaging. *Angew. Chem. Int. Ed. Engl.* **49**, 2711–2715 (2010).
27. Chong, P. S. & Finlay, I. G. Surgical options in the management of advanced and recurrent colorectal cancer. *Surg. Oncol.* **16**, 25–31 (2007).
28. Chokshi, R. J., Abdel-Misih, S. & Bloomston, M. Surgical management of colorectal cancer: a review of the literature. *Indian J. Surg.* **71**, 350–355 (2009).
29. Mocellin, S. *Microarray Technology and Cancer Gene Profiling. Advances in Experimental Medicine and Biology* (Springer, 2007).
30. Adiconis, X. *et al.* Comparative analysis of RNA sequencing methods for degraded or low-input samples. *Nature Methods* **10**, 623–629 (2013).
31. Hemmat, M. *et al.* Short stature, digit anomalies and dysmorphic facial features are associated with the duplication of miR-17~92 cluster. *Mol. Cytogenet.* **7**, 27 (2014).
32. Lu, J. *et al.* MicroRNA expression profiles classify human cancers. *Nature* **435**, 834–838 (2005).
33. Mendell, J. T. miRiad roles for the miR-17-92 cluster in development and disease. *Cell* **133**, 217–222 (2008).
34. Hatakeyama, H. *et al.* A DNA microarray-based analysis of the host response to a nonviral gene carrier: a strategy for improving the immune response. *Mol. Ther.* **19**, 1487–1498 (2011).
35. Meerzaman, D. M. *et al.* Genome-wide transcriptional sequencing identifies novel mutations in metabolic genes in human hepatocellular carcinoma. *Cancer Genomics Proteomics* **11**, 1–12 (2014).
36. Voloshanenko, O. *et al.* Wnt secretion is required to maintain high levels of Wnt activity in colon cancer cells. *Nature Commun.* **4**, 2610 (2013).
37. Herath, N. I., Doecke, J., Spanevello, M. D., Leggett, B. A. & Boyd, A. W. Epigenetic silencing of EphA1 expression in colorectal cancer is correlated with poor survival. *Br. J. Cancer* **100**, 1095–1102 (2009).
38. Kok-Sin, T. *et al.* Identification of diagnostic markers in colorectal cancer via integrative epigenomics and genomics data. *Oncol. Rep.* **34**, 22–32 (2015).

Acknowledgements

J.C. acknowledges Marie Curie International Outgoing Fellowship and Funding (FP7-PEOPLE-2013-IOF, Project 626386). We thank the Swanson Biotechnology Center at the Koch Institute for Integrative Cancer Research at Massachusetts Institute of Technology (MIT) for assistance with animal experiments and facilities, especially the microscopy, flow cytometry, and histology cores. We also acknowledge that all qPCR and microarray experiments done in the KI Genomics Core/MIT BioMicro Center are funded by the NIH and supported in part by the Koch Institute Support Grant P30-CA14051 from the National Cancer Institute and by the National Institute of Environmental Health Sciences of the NIH under award P30-ES002109. We thank D. Ma and C. Whittaker from the Bioinformatics and Computing Core Facility at David H. Koch Institute for Integrative Cancer Research at MIT for the microarrays analysis. We thank D. S. Yun for cryo-TEM assistance at the Peterson Nanotechnology Materials Core Facility. We thank the Department of Comparative Medicine at MIT, especially J. Haupt. We thank G. Paradis for FACS assistance with Cancer Center Support (FACS core) Grant P30-CA14051 from the National Cancer Institute. We thank P. Boisvert and Y. Zhang for technical assistance in SEM at the MIT Center for Materials Science and Engineering (CMSE). These SEM studies made use of the MRSEC Shared Experimental Facilities at MIT, supported by the National Science Foundation under award number DMR-1419807.

Author contributions

J.C. and N.A. conceived the project and designed the experiments. J.C. and N.O. performed the experiments, and collected and analysed the data. Y.Z. performed the SEM studies. J.C. and N.A. co-wrote the manuscript. All authors discussed the results and reviewed the manuscript.

Additional information

Supplementary information is available in the online version of the paper. Reprints and permissions information is available online at www.nature.com/reprints. Correspondence and requests for materials should be addressed to J.C. or N.A.

Competing financial interests

The authors declare no competing financial interests.

Methods

Synthesis and characterization of gold nanorods and nanospheres. All of the details regarding the synthesis and characterization of the drug–gold nanorods and siRNA–gold nanospheres for local gene and drug release in colorectal cancer (CRC) cells can be found in the Supplementary Information. General characterization of the nanoconjugates and hydrogel scaffolds was performed by dynamic light scattering (Wyatt Dyna Pro Plate Reader), zeta potential (Zetasizer Nano-ZS90 Malvern), fluorescence and ultraviolet/visible spectroscopy and environmental scanning microscopy (FEI/Philips XL30 FEG ESEM) and high-resolution cryo-TEM (JEOL 2100 FEG TEM).

***In vitro* nanorod and nanosphere delivery.** LoVo-6-Luc-1 CRC cells (PerkinElmer, tested for mycoplasma contamination by the Division of Comparative Medicine Diagnostic Laboratory at MIT via IMPACT PCR and found to be negative; the parental cell line was authenticated and certified free of interspecies cross-contamination by short tandem repeat profiling) were grown in Ham's F12 medium (Invitrogen) supplemented with 4 mM glutamine, 10% heat-inactivated fetal bovine serum (Gibco, Life Technologies), 100 U ml⁻¹ penicillin and 100 µg ml⁻¹ streptomycin (Invitrogen) and maintained at 37 °C in 5% CO₂. Cells were seeded at a density of 1 × 10⁵ cells per well in 24-well plates and grown for 24 h before incubation of gold nanorods and nanospheres (10 nM each). On the day of incubation, the cells were approximately 50% confluent. For confocal microscopy, cells were fixed with 4% paraformaldehyde in PBS for 15 min at 37 °C and stained with DAPI to allow nuclear staining and finally mounted in ProLong Diamond Antifade Reagent (Invitrogen). Images of cells were taken with a Nikon A1R Ultra-Fast Spectral Scanning Confocal Microscope.

Flow cytometry. LoVo-6-Luc-1 CRC cells incubated with 10 nM drug–gold nanorods and siRNA–gold nanospheres were washed with PBS and detached with 0.25% trypsin–EDTA (Life Technologies). FACS running buffer (500 µl), consisting of 98% PBS and 2% heat-inactivated fetal bovine serum (Gibco, Life Technologies), was added to each well. Cells were mixed thoroughly and then transferred to a FACS tube with a filter lid, and the Alexa Fluor 555 (from gold nanorods) and DY647 (from gold nanospheres) signals were acquired on a FACS LSR Fortessa HTS-1 (BD Biosciences) flow cytometer.

Cell viability and proliferation assays. A standard MTT (3-(4,5-dimethylthiazol-2-yl)-2,5-diphenyltetrazoliumbromide) reduction assay (Molecular Probes, Life Technologies) was performed to determine the viability of cells to increasing concentrations of drug–gold nanorods and siRNA–gold nanospheres. Cells were seeded at a density of 1 × 10⁵ cells per well in 24-well culture plates in complete Ham's F12 medium (500 µl) with serum. After 24 h of exposure to gold nanorods and nanospheres, the medium was removed and the cells were washed twice with sterile PBS, and 300 µl of fresh medium with serum was added. Then 16.7 µl of sterile MTT stock solution (5 mg ml⁻¹ in PBS) was added to each well. After incubation for an additional 2 h, the medium was removed and the formazan crystals were resuspended in 300 µl of dimethyl sulfoxide (Sigma). The solution was mixed and its absorbance was measured at 540 nm as a working wavelength and 630 nm as a reference using a microplate reader (Varioskan Flash Multimode Reader, Thermo Scientific). The cell viability was normalized to that of cells cultured in the culture medium with PBS treatment.

For the dead–live assays, the treated cells were incubated for 30 min with acridine orange (Sigma), which stains live cells, at a final concentration of 0.67 µM, and with propidium iodide (Sigma), which stains apoptotic/dead cells, at a final concentration of 75 µM. Then cells were washed 2 × with PBS 1 × and images of the cells were taken either with a Nikon A1R Ultra-Fast Spectral Scanning Confocal Microscope or with a Nikon Eclipse Ti Epi-fluorescence Microscope.

Development of CRC mice model. Subcutaneous tumours were induced in male SCID hairless congenic mice (SHC Mouse CB17.Cg-Prkdc^{scid}HR^{hr}/IcrCrl from Charles River Laboratories International, 6 weeks, *n* = 5) by injection of 5 × 10⁶ LoVo-6-Luc-1 CRC cells stably expressing firefly luciferase, suspended in 50 µl of HBBS (Lonza) solution. For determination of tumour growth, individual tumours were measured using a calliper and tumour volume was calculated as: tumour volume (mm³) = width × (length²)/2. Treatments began when the tumour volume reached about 100 mm³. All experimental protocols were approved by the MIT Animal Care and Use Committee and were in compliance with NIH guidelines for animal use.

Quantitative PCR for gene expression. Total RNA from LoVo-6-Luc-1 CRC cells and respective tumours from SCID hairless congenic mice was extracted using the RNeasy Plus Mini Kit (Qiagen) according to the manufacturer's protocol. cDNA was produced using the High-Capacity cDNA Reverse Transcription Kit (Applied Biosystems) using 500 ng of total RNA. qRT-PCR was performed with Taqman probes FAM-MGB for *Kras*, *VEGF*, *SFRP4*, *ANK1*, *CTNNA2*, *EPHA1* and *DEFB119*. *GAPDH* was used as a reference gene. The reactions were processed using a Light Cycler 480 II Real-time PCR machine (Roche) using TaqMan Gene

Expression Master Mix (Applied Biosystems) under the following cycling steps: 2 min at 50 °C for UNG activation; 10 min at 95 °C; 40 cycles at 95 °C for 15 s; 60 °C for 60 s. At least three independent repeats for each experiment were carried out. Gene expression was determined as a difference in fold after normalizing to the housekeeping gene *GAPDH*.

Gold nanorod and nanosphere hydrogel scaffold synthesis and *in vivo* implantation and injection. Tagged hydrogel scaffolds were developed as previously described^{11,24}. Briefly, equal parts of dendrimer amine of 12.5% solid content and dextran aldehyde 5% solid content with 0.25% fluorescently labelled dextran were mixed to form 6 mm pre-cured discs. For doped scaffolds, 10 nM drug–gold nanorods and 10 nM siRNA–gold nanospheres were added to the dendrimer solution before hydrogel formation. All solutions were filtered through a 0.22 µm filter before hydrogel formation for *in vivo* implantation. Pre-cured discs of fluorescently labelled scaffold with or without RNA nanoparticles were formed and implanted subcutaneously on top of the mammary tumour in mice. For systemic administration, 10 nM of drug–gold nanorods and 10 nM siRNA–gold nanospheres was injected into mice via the tail vein, and for intratumoural administration 10 nM of drug–gold nanorods and 10 nM siRNA–gold nanospheres was injected directly into the tumour.

Dextran aldehyde tagging reaction. Dextran aldehyde (*M*, 10,000 Da, 50% oxidation; 10 mg) was tagged by reaction with 2 mg Alexa Fluor 405 cadaverine (Invitrogen) in 20 ml of 50 mM carbonate buffer (pH 8.5) for 1 h at room temperature. Then, the reaction crude was cooled down in an ice-water bath and imine bonds were reduced with 20 ml of 30 mM sodium cyanoborohydrate in PBS for 4 h. Then, tagged dextran aldehyde was dialysed four times through a 3,000 Da MWCO centrifugal filter (Millipore) for 20 min each time at room temperature and 4,000 RCFs. The purified product was lyophilized.

Gold nanorod and nanosphere release from hydrogel scaffold *in vitro*. Pre-cured discs of fluorescently labelled hydrogel scaffold alone or doped with gold nanorods and nanospheres were incubated in phosphate-buffered saline (PBS) at 37 °C. At different time points, samples were collected from the PBS and fluorescence of released products was quantified (Varioskan Flash Multimode Reader, Thermo Scientific). Data were plotted as the percentage of total nanoparticles or dextran aldehyde released for each time point. Controls for this experiment included empty scaffold (without nanoparticles).

Gold nanorod and nanosphere hydrogel scaffold fluorescence images. Pre-cured fluorescently labelled scaffolds alone (control) or doped with drug–gold nanorods and siRNA–gold nanospheres were snap-frozen in liquid nitrogen and kept at –80 °C for 24 h. Then, 12-µm-thick cryosections (Cryostat Leica CM1850) were analysed by fluorescence microscopy (NIS-Elements Nikon). Controls for this experiment included empty scaffold (without nanoparticles).

Analysis of tumour growth and gold nanorod and nanosphere hydrogel scaffold degradation. Non-invasive longitudinal monitoring of tumour progression was followed by scanning mice with the IVIS Spectrum-bioluminescent and fluorescent imaging system (Xenogen XPM-2 Corporation) from mice bearing colorectal tumours (*n* = 5 animals per treated group). Fifteen minutes before imaging, mice were intraperitoneally injected with 150 µl of D-luciferin (30 mg ml⁻¹, Perkin Elmer) in DPBS (Lonza). Whole-animal imaging was performed at the indicated time points—1, 5, 8 and 15 days after hydrogel disc implantation, and at 1, 3 and 10 after NIR application (120 s exposure during four sessions). Assessment of *in vivo* toxicity via mice body weight evaluation was performed on all of the animal groups during 35 days after tumour induction and 15 days after hydrogel implantation. Histological sections of the tumours (*n* = 5) were stained with haematoxylin and eosin and for immunohistochemical analysis the tumours (*n* = 5) were stained with the antibody anti-Ki67 (Abcam ab15580, dilution 1:200). Quantification of the fluorescence signal of the tumours from mice treated with hydrogel containing the triple therapy was performed over time (6, 24, 48, 72 h and 15 days). The total fluorescence of the nanoparticles in the tissue was assessed by the sum of all pixel intensities for each colour channel (red for the gold nanospheres (DY647 dye) and green for the gold nanorods (Alexa Fluor 555)). During the image analysis the photons that are collected at each pixel are converted into pixel intensities using ImageJ software (version 1.49). Therefore, the sum of all pixel intensities in a region is proportional to the amount of particles in that region.

Gene expression analysis. Total RNA from colorectal tumours was extracted using the RNeasy Plus Mini Kit (Qiagen) according to the manufacturer's protocol. RNA integrity was checked using the AATI Fragment Analyzer. Samples for the arrays were prepared using the Nugen Applause 3' Amp kit and were hybridized to the Affymetrix GeneChip PrimeView Human Gene Expression Array. For gene expression heat maps, the average expression across three replicates in each condition based on the probes with the maximum signal intensity per gene was calculated. Heat maps were created using Genesis 1.7.6³⁹. Pearson correlations were

analysed using R 2.15.3. Scatter plots were also made by R 2.15.3. Heat maps were created by Genesis 1.7.6 based on Pearson correlation coefficients of each replicate per condition.

Gene ontology and pathway analysis. Pathway analyses were performed using Gene Set Enrichment Analysis tool v2.0.13 (GSEA2-2.0.13)^{40,41}. The analyses were based on differentially expressed genes in each treatment group including phototherapy, gene therapy, chemotherapy or the triple-therapy combination compared with sham controls. Differential expression was defined as multiple testing adjusted p values smaller than or equal to 0.05 and fold change greater than or equal to 1.5-fold by probes with the maximum intensity in each gene. The enrichment results with canonical pathway gene sets C2CP were reported. FDR 25% or less was used to select interesting gene sets for hypothesis generation.

Statistics. Differences between groups were examined using a two-tailed Student's t -test, two-way analysis of variance or a Log-Rank Mantel–Cox test through the SPSS statistical package (version 23, SPSS). All error bars used in this report are mean \pm s.d. of at least three independent experiments. Statistically significant

p values are indicated in figures and/or legends as ***, $P < 0.005$; **, $P < 0.01$; *, $P < 0.05$. All *in vivo* experiments used five mice per treatment group. A power analysis was performed using G*Power software (version 3.1.9.2) to determine sample size. For $n = 5$ mice per group the power is 90% with a signal-to-noise ratio of 2.4, assuming a 5% significance level and a two-sided test. The signal/noise ratio of 2.4 corresponds to a 6.1% background signal. No randomization or blind events were used in animal studies.

References

39. Sturn, A., Quackenbush, J. & Trajanoski, Z. Genesis: cluster analysis of microarray data. *Bioinformatics* **18**, 207–208 (2002).
40. Mootha, V. K. *et al.* PGC-1 alpha-responsive genes involved in oxidative phosphorylation are coordinately downregulated in human diabetes. *Nature Genet.* **34**, 267–273 (2003).
41. Subramanian, A. *et al.* Gene set enrichment analysis: a knowledge-based approach for interpreting genome-wide expression profiles. *Proc. Natl Acad. Sci. USA* **102**, 15545–15550 (2005).